Enhanced radiation tolerance of nanochannel V films through defects release

CrossMark

Hongxiu Zhang [a], Feng Ren [a],*, Yongqiang Wang [b], Mengqing Hong [a], Xiangheng Xiao [a], Dan Liu [a], Wenjing Qin [a], Xudong Zheng [a], Yichao Liu [a], Changzhong Jiang [a],*

[a] School of Physics and Technology, Center for Ion Beam Application and Center for Electron Microscopy, Wuhan University, Wuhan 430072, PR China
[b] Materials Science and Technology Division, Los Alamos National Laboratory, Los Alamos, NM 87545, USA

ARTICLE INFO

ABSTRACT

Since surfaces are perfect sinks for defects, nanochannel material with a high surface to volume ratio has the potential to be extremely radiation tolerant. Nanochannel V films deposited at 500 °C and 600 °C, Ag and V/Ag multilayer films deposited at room temperature and bulk V, were subjected to He irradiation. TEM images show larger bubbles appeared in the Ag film and the V/Ag multilayer under He$^+$ ion irradiation to a fluence of 5×10^{16} ions/cm^2. While few small He bubbles formed in the irradiated nanochannel V film and a high density of small bubbles appeared in the irradiated bulk V when the fluence of He$^+$ ions reaches 1×10^{17} ions/cm^2, which is two times higher than the fluences on the Ag and multilayer films. Radiation-induced defects can quickly diffuse to the free surfaces of the nanochannels, which greatly reduces the concentration of defects in material and increases the radiation tolerance. Radiation hardening is observed in all specimens. The irradiation-induced hardening in the V nanochannel films is around one third to one fourth of that in the bulk V.

© 2014 Elsevier B.V. All rights reserved.

1. Introduction

Advanced nuclear power systems are being designed with the potential to make significant contributions to future energy demands in an environmentally acceptable manner. The safe, reliable and economic operation of such nuclear plants will be critically dependent on good materials performance. In fission and fusion reactors, a large quantity of helium will be generated in structural materials as a result of (n, α) transmutation reactions or by direct injection into the near surface region of the first wall. Due to its extremely low solubility in metals (below the ppm level), for helium concentrations above the solubility limit, helium tends to cluster and precipitate in the form of bubbles [1–4]. The formation of He bubbles enhances swelling, embrittlement and eventually leads to the failure of the plasma-facing materials and structural materials [5–7]. Extending the operating limits and lifetimes of nuclear reactor materials through manipulating the behavior of defects in materials is an urge target. It requires the ability to decrease the effects of radiation-induced damage, particularly to prevent the degradation of material properties due to the growth of bubbles and the subsequent formation of blisters [3,8]. Atomistic

simulations and experiments have proved that one way to suppress the accumulation of point defects in irradiated materials is to annihilate freely-migrating point defects at sinks, such as free surfaces, interfaces [9–12]. Therefore, materials fabricated by different strategies were explored to achieve radiation tolerance, e.g. using nanoscale multilayers [4–8,12–15], oxide dispersion strengthened (ODS) steels [16], nanofoam materials [17,18]. It should be noted, the properties of free surfaces with high efficiency for trapping and releasing defects are substantially different from the properties of the interfaces or grain boundaries in nanocrystalline solids: the presence of free surfaces create image forces that introduce a driving force enhancing defect migration, increasing the sink strength compared to interfaces in compact materials [17]. Therefore, nanochannel materials are supposed to have better anti-irradiation performance than multilayers, nanocrystal composites. Vanadium and its alloys are candidates for the structural material of fusion reactors due to their low activation property, high refractory, high-temperature strength and high thermal stress factor, and high compatibility with liquid Li as the tritium breeder and coolant [19–22].

In the present work, we develop a new strategy to release defects using nanochannel V films with rich free surfaces. Structural characterizations of the as-deposited and the irradiated samples by transmission electron microscopy (TEM) show that few

* Corresponding authors. Tel.: +86 27 68752567; fax: +86 27 68752569.
E-mail address: fren@whu.edu.cn (F. Ren).

bubbles are formed in the nanochannel V films, while numerous bubbles appear in the bulk V, Ag and V/Ag multilayer films. Nano-channel films are proved to be highly radiation tolerant.

2. Experimental

V nanochannel films with thicknesses of 450 nm were deposited onto Si (1 0 0) wafers at 500 °C and 600 °C (named as nanochannel V500 and nanochannel V600, respectively) using an ultra high vacuum magnetron sputtering system (ULVAC, ACS-4000-C4). Ag film and V/Ag multilayer film (the individual layer thicknesses were 6 nm for both Ag and V) were also deposited for comparison. The deposition rates were 4 nm min^{-1} for V and 20 nm min^{-1} for Ag. The nanochannel V films and bulk V were irradiated at room temperature by 40 keV He$^+$ ions with a tilt angle of 7° to a fluence of 1×10^{17} ions/cm^2. The Ag film and the V/Ag multilayer were irradiated at the same energy to a fluence of 5×10^{16} ions/cm^2. Nano-hardness tests were performed by continuous stiffness measurement (CSM) method in a type Nano Indenter G200 (American MTS Corporation). The maximum load was 60 mN, and the indentation depth was 450 nm. The average hardness value and the standard deviation were determined from 6 indents on each specimen. In this way, the possible deviation of the measurement induced by surface roughness or un-uniformity of the film can be reduced and more accurate values can be achieved.

3. Results and discussion

3.1. Microstructural evolution

Fig. 1 shows the cross-sectional SEM images of the as-deposited Ag and the nanochannel V films. The Ag film showed a layered structure with a flat surface, while the growth of V films was mainly dominated by island nucleation mechanism. Grain boundaries formed by island coalescence during deposition have very low mobility even at a substrate temperature as high as 1/3 T_m (T_m is the melting temperature of V). The surfaces of the V nanochannel films were uneven due to the crystal columns, while the surface of the Ag film was flat due to the layered structure. The reasons account for the columnar structure of the V films include high surface energy of V [23–28] and shadowing effect due to the non-normal incidence of sputtering flow [29,30]. It can also be seen that the film density was largest for the Ag film, moderate for the nanochannel V500 and smallest for the nanochannel V600.

Fig. 2a and b show the cross-sectional TEM images of the Ag and V/Ag multilayer films irradiated by 40 keV He$^+$ ions to a fluence of 5×10^{16} ions/cm^2. SRIM simulation indicated that the He concentration was 6 at.% at a depth of around 135 nm underneath the film surface and the peak displacement per atom (dpa) was approximately 6 at a depth of 110 nm in the Ag film. He bubbles were observed in the Ag film, which appearing as white dots surrounded by a dark Fresnel fringe. The bubbles with a broad size distribution ranging from 1.8 to 14 nm were not only in the grain interior but also at the grain boundaries. Larger bubbles are mainly distributed along the grain boundaries. The average diameter of the He bubbles in the Ag film was 3.2 ± 1.6 nm. For the irradiated V/Ag multilayer in Fig. 2b, discrete layer structure is retained. SRIM simulation indicated that the He concentration was 5 at.% at a depth of 150 nm and the peak dpa was 5 in Ag layers and 4 in V layers. From Fig. 2b, it can be seen that: (1) He bubbles are densely packed along the V and Ag interfaces; (2) larger bubbles prefer to form in Ag layers; (3) the average diameter of the bubbles is 2.2 ± 0.7 nm, smaller than that of 3.2 ± 1.6 nm in the Ag film, indicating that the bubble size can be suppressed by the multilayered
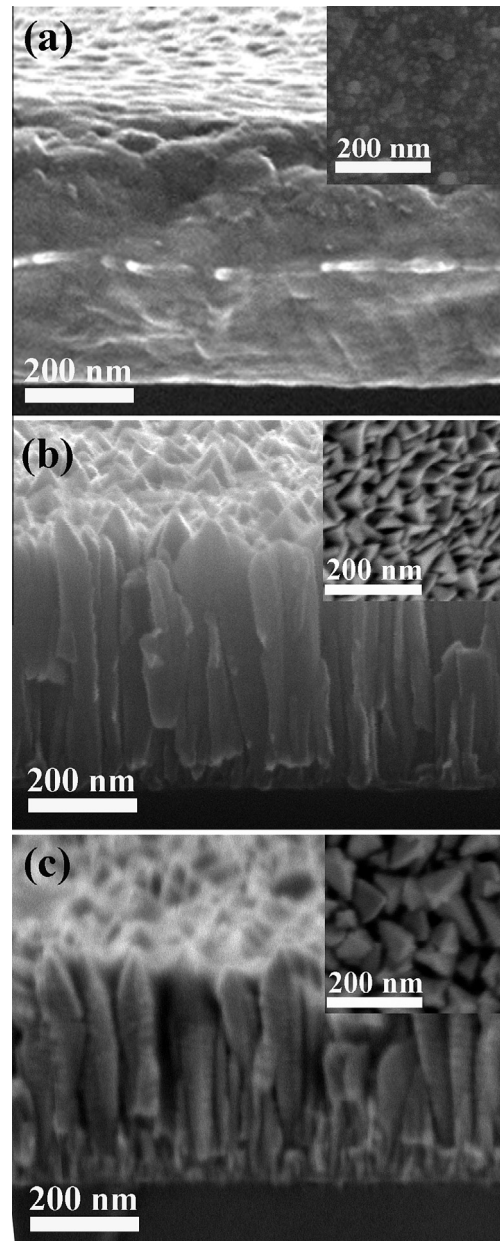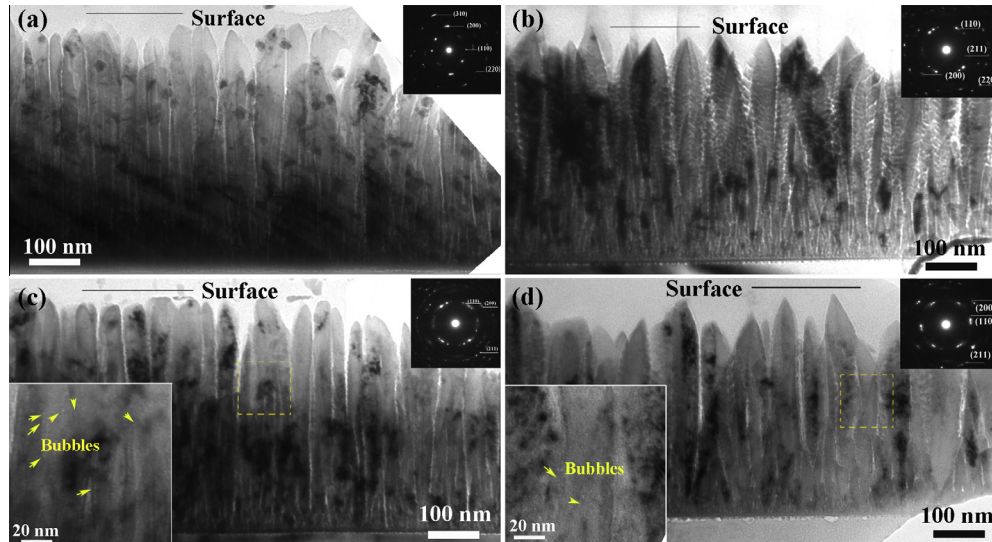

Fig. 1. Cross-sectional SEM images of the Ag (a), nanochannel V500 (b) and nanochannel V600 (c) films. Insets show the corresponding plan-view images.

structure. The reason for the formation of large numbers of bubbles along the interfaces has been well studied. Briefly, it is due to the interaction between interface stress field and stress along He bubbles [5]. The misfit dislocation spacing in the V, Ag interface was on the order of a few nanometers, indicating a high population of defect trapping sites in the interface plane [31,32]. As a consequence, a high density of vacancies was generated at interfaces that would tend to further trap the helium at interfaces. Therefore, large numbers of bubbles were distributed at the interfaces. The decreased bubble size in the multilayer compared with that in Ag film was due to the confinement of the interfaces [32]. The results clearly show that compared with traditional material such as Ag film, multilayer film has higher ability to handle He and other defects. Fig. 2c shows the radiation damage of bulk V, which was irradiated by 40 keV He$^+$ ions to a fluence of 1×10^{17} ions/cm^2. The He concentration was 10 at.% at the depth of 190 nm and the dpa was 9 at the depth of 150 nm. The uniformly distributed
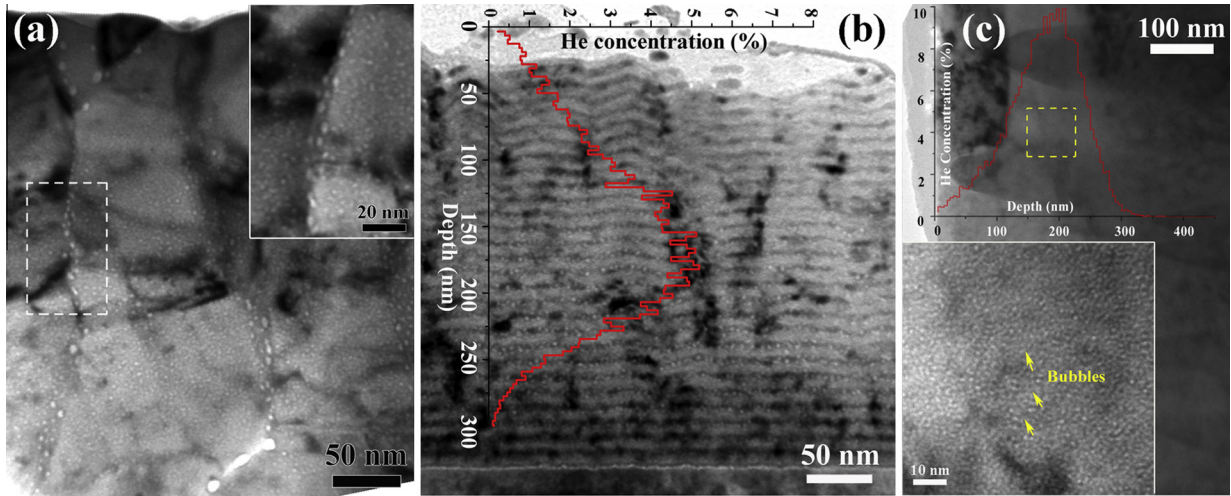
Fig. 2. Cross sectional TEM images of the 40 keV He[+] ion irradiated Ag film (a), V/Ag multilayer film (b) to a fluence of 5×10^{16} ions/cm^{2} and the irradiated bulk V (c) to a fluence of 1×10^{17} ions/cm^{2}. The curves in (b) and (c) are the calculated (SRIM) results for He concentration versus depth. The magnified images of the dashed boxes in (a) and (b) are also attached.

Fig. 3. Cross-sectional TEM images of the as-deposited nanochannel V500 (a), V600 (b) and the 40 keV He[+] ion irradiated nanochannel V500 (c), V600 (d) to a fluence of 1×10^{17} ions/cm^{2}. Insets is the local magnified TEM images of the boxes. Corresponding SAED patterns are shown in the upper right of each image.

bubbles with diameter around 1 nm can be found in the damaged area in V. A significant difference exists in radiation damage between fcc and bcc structure subjected to the same radiation conditions [32,33]. The differences of the bubbles in Ag and V originate from the difference in surface energy between Ag and V according to the relationship: $P = 2\gamma/r$, where P is the pressure of the bubble, γ is the surface energy, and r is the radius of He bubble [4,32]. Other factors also account for the differences of bubble formation between bcc V and fcc Ag, including: fewer vacancies were produced for each cascade in V than in Ag; the vacancies in V surviving from the cascades were prefer to be presented as isolated ones instead of aggregation; higher threshold for punching interstitial loops and lower mobility of trapped He at ambient temperatures in V [32].

Fig. 3 is the cross-sectional TEM images for the nanochannel V500 and V600 before and after irradiation. From Fig. 3a and b, we can see both of the nanochannel V500 and V600 showed a nanochannel structure with column sizes of 41 and 58 nm,

respectively. For the nanochannel V500, the relative density was 85%. Low density of He bubbles around 1 nm were formed within the columnar grains of the irradiated nanochannel V500, as indicated by arrows in the magnified TEM micrograph. The size and density of He bubbles in the nanochannel films is smaller and lower than that in the Ag and V/Ag multilayer films, although the irradiation fluence was two times higher. The selected area electron diffraction (SAED) images indicate that irradiation with a high fluence did not amorphize the nanochannel V500. Fig. 3b and d show the TEM images of nanochannel V600 before and after irradiation. The difference of the structure characteristics between the as-deposited nanochannel V500 and V600 is that in the latter, there are even small nanochannels in the columns. Here, we name such nanochannel structure as "vein-like" nanochannel, which leads to a low density of 75% of the V600. It was also interested to find that the "vein-like" nanochannels were disappeared after irradiation, and the relative density increased to 87%. In addition, fewer bubbles formed in the irradiated nanochannel

V600 comparing with the irradiated nanochannel V500. For the nanochannel V500 and V600 irradiated by He⁺ ions to a fluence of 5×10^{16} ions/cm², no visible bubbles were observed in both samples.

To figure out the detailed mechanism for the enhanced radiation tolerance of the nanochannel V films, we firstly present the process of the formation and the evolution of defects during irradiation. The radiation process can be divided into two stages. In the first stage of defect production at the atomic-level ($\sim10^{-15}$ s, $\sim10^{-10}$ m), point defects are created in the collision cascade process. The second stage is the stability, mobility and interaction of the defects created in the first stage over the mesoscale ($\sim10^{-6}$ s, 10^{-3} m) [34,35]. The latter stage is important for the radiation tolerance of materials, because the interaction and migration of such defects are critical in governing the microstructural evolution, which in turn determines the degradation of the macroscopic properties of the materials. The structural, mechanical and chemical properties of materials change over long time scales as a result of damage accumulation and evolution. Eventually, void swelling, irradiation creep, hardening, and chemical segregation occur in the material. If the point defects such as He interstitials, vacancies can diffuse to the surface between two sequential cascades, there will be no defect accumulation.

Below we estimate more quantitatively the maximum He releasing capability of the nanochannel V films from the point of view of diffusion rate. We firstly discuss the diffusion behavior of He interstitials. The diffusion distance L of the He can be expressed by the Eq. (1) [18,36–38].

$$L = \sqrt{D\tau} \tag{1}$$

where D is the diffusion coefficient, τ is the time between two successive incoming He⁺ ions. The diffusion coefficient of He in vanadium can be evaluated by the Arrhenius diffusion Eq. (2).

$$D = D_0 \exp(-E_a/k_B T) \tag{2}$$

where D_0 is diffusion constant, k_B is Boltzmann constant, T is absolute temperature, E_a is activation energy. The main diffusion path of He is the direct hopping path between two nearest-neighbor tetrahedral sites. The diffusion barriers is 0.06 eV with the diffusion constants (D_0) of 3.04×10^{10} nm²/s. According to Eq. (2), the diffusion coefficients is $D = 3 \times 10^9$ nm²/s. An estimate of He diffusion distance can be obtained by assuming that collision cascades occur within a $a \times a \times a$ cube, a represents the column size of V films. The time between two successive incoming He⁺ ions depends on the flux. For a given He⁺ ion flux, the material will not continually accumulate new defects to form larger defect clusters (e.g. He bubbles) if the diffusion length L by which the defects migrate in the interval time of two successive cascades is larger than the half of the size of crystal column. Fig. 4 shows the difference (ΔL) between $a/2$ nm and the calculated diffusion distances under different He ion fluxes as a function of the cube size a. The He⁺ ion flux in this experiment was 3.75×10^{13} ions/(cm² s). The upper size of the column was 424 nm, suggesting that if the column size was smaller than 424 nm, continuous He outgassing through nanochannels by diffusion alone was sufficient. The small column size induced by the "vein-like" structure of V600 was 15 nm, it could be radiation tolerant up to a He ion flux of 2.37×10^{19} ions/cm²/s, which was in the level of the He ion flux near the edging fusion plasma encountered by first wall materials ($\sim10^{19}$ ions/cm²/s). For the V500 with the average column size of 40 nm, it could be radiation tolerant up to a He ion flux of 4.69×10^{17} ions/cm²/s. Kiritani et al. [39] studied the neutron irradiation on thin foil Ni. The foil was wedge-shaped with gradually increased thickness from top to bottom. After irradiation, different defect microstructures formed in the foil with different foil thickness. In the thinnest part, no defect structures
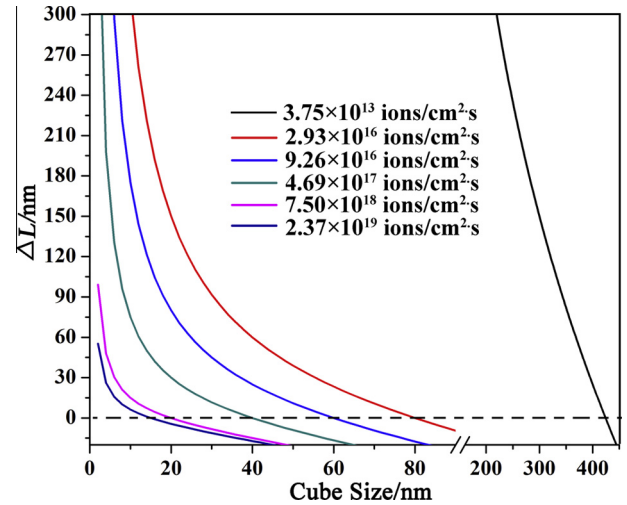

Fig. 4. Schematic curves for the difference (ΔL) between $a/2$ and the diffusion distances under different He⁺ ion fluxes as a function of the cube size.

developed because of the escape of all the freely migrating point defects to specimen surfaces. Voids, dislocations formed in the parts that are thick enough [39]. The variations of point-defect concentration with irradiation time were presented basing on the kinetics formulation of point defects [40].

Displacement cascades produce large densities of SIAs [41], which can form dislocation loops and cause hardening. The energy barrier for SIA motion is low and in the range of 0.01–0.06 eV [36,37,39,41–44]. The diffusion coefficients were calculated to be $2.5–20 \times 10^9$ nm²/s [37,42,45]. In a time of 7×10^{-4} s, the corresponding diffusion length was 1300–3700 nm. The diffusion distances were far beyond the column size of the V nanochannels. This was in accordance with the simulation results by Bai et al. [9]. Thus, interstitials could move rapidly to the free surfaces of nanochannels. The disappeared vein-like nanochannel structure of the irradiated nanochannel V600 was caused by the rapid migration and filling of He atoms and V interstitial atoms.

He⁺ ion irradiation also produces vacancies in the materials. The migration barrier for vacancy is high (0.5–1.2 eV) [36,43,46]. The high barrier value of vacancy is many times higher than $k_B T$ (0.026 eV). According to the Eq. (2), the exponential factor is very small ($\exp(-E_a/k_B T) \ll 1$) [36], and the vacancies can not diffuse to the surface in a short time. However, as large numbers of interstitials diffuse to the surfaces, the interstitial-loaded surfaces can affect the vacancy diffusion barrier. Bai et al. [9] simulated the diffusion behavior of vacancy and found that compared with the perfect grain boundaries, the interstitial-loaded grain boundaries reduced the vacancy diffusion barrier considerably from 0.7 eV to 0.3 eV as the distance between the vacancy and grain boundary reduced. Then, the diffusion coefficient of vacancy in V was calculated to be 2.37×10^6 nm²/s, using the reduced migration energy [45], and resulting in a diffusion length of 40 nm according to Eq. (1). In addition, when the vacancies were near the interstitial-loaded grain boundaries, interstitial emission with low barriers occured, which could annihilate the vacancies nearby. The remaining vacancies inside the columns catched He atoms and formed He-vacancy clusters and He bubbles which were observed in Fig. 3c and d. In the nanochannel V500, according to the calculation above, the widely distributed nanochannels released the implanted He atoms and result in a great decrease of the bubble density.

As mentioned above, He impurities can easily diffuse to the vacancy sites, forming He–vacancy complexes. The activation energy of a vacancy–helium complex (over 2.21 eV) would be considerably high. Therefore, the vacancy–helium complex has a quite

low thermal mobility in vanadium [46]. At room temperature, the function of radiation induced motion would be comparable to that of thermal motion and can not be neglected. The formation of divacancies in the irradiated metals at a low temperature, at which the thermal motion of vacancies is not expected at all, confirms the effect of radiation induced diffusion [40,47]. The collision cross-section to transfer the energy required for the diffusion of point defects were calculated by Kiritani [48]. The radiation effect on the displacement of defects was in general larger for defects with smaller migration energy. Sun et al. found that various types of defect clusters could be removed by the free surfaces and grain boundaries of the nanoporous Ag [49]. Different from the vacancy–helium complex, which has a strong attractive interaction, a repulsive interaction was found for helium–SIA cluster. The binding energy is minus (–0.37 eV), implying that self interstitial defects are unable to trap He atom directly [50].

It should be noted that the calculations of the diffusion length of the helium, interstitials and vacancies did not consider the effect of the defects. For the microstructure of the V nanofilms, the TEM images and SAED patterns of them indicated that the films were polycrystalline with abundant free surfaces. The high resolution TEM image indicated that there were grain boundaries between the V grains and few dislocations were observed in the films. However, dislocations were inevitable in the irradiated films. Both grain boundaries and defects such as dislocations would capture the partial of helium, interstitials and vacancies and affect their diffusion. This is the reason why small he bubbles are still observed in the nanochannel films. In addition, the image force induced by the free surfaces was not considered in the calculation of the diffusion length of the defects. The image force provide driving force for the migration of defects towards free surface.

In the nanochannel V500, according to the calculation above, the widely distributed nanochannels could release the implanted He atoms and resulted in a great decrease of the bubble density. In the nanochannel V600, the density of He bubbles was further reduced through the vein-like nanochannel structure, which accelerated the diffusion process. Therefore, a reduced number of bubbles were observed in the nanochannel V600. In the case of the bulk V, the V/Ag multilayer and the Ag films irradiated by He$^+$ ions, as lack of effective diffusion mechanism, the deposited He atoms could agglomerate themselves or in the irradiation-induced vacancies to become the nucleus for He bubble formation [4]. In addition, the solubility of He in the bulk V and the Ag film is negligible, bubbles can form at extremely low concentration of He. Therefore, large numbers of He bubbles formed in the irradiated bulk V, V/Ag multilayer and Ag films. In conclusion, the nanochannel V films have high He bubble management ability and could be unusually resistant to radiation because radiation-induced point defects could not accumulate in the presence of the high density of defects sinks provided by the free surfaces of the nanochannels.

3.2. Mechanical properties

Radiation induced defects can aggregate to form dislocation loops, stacking-fault tetrahedras or cavities, leading to irradiation hardening. Radiation hardening typically occurs with embrittlement and is generally considered as a gauge to probe the magnitude of radiation damage [14]. Table 1 lists the hardness with standard deviation measured for the tnanochannel V films and the bulk V before and after He$^+$ ion irradiation at the same fluence. The indentation data was extracted from an indent depth of less than 100 nm at which a platform exists in the hardness VS penetration depth plot. According to the TEM image and the SRIM simulation, extracting hardness at depths <100 nm ensures that we capture the effects of He implantation damage and avoid substrate

Table 1
Hardness of specimens before and after irradiation.

Samples	As-deposited hardness (Gpa)	As-irradiated hardness (Gpa)	Difference hardness (Gpa)
Bulk V	2.9 ± 0.1	5.4 ± 0.2	2.5
Nanochannel V500	3.9 ± 0.2	4.8 ± 0.3	0.9
Nanochannel V600	2.9 ± 0.2	4.2 ± 0.1	1.3

effects. There are two points need to be noted. Firstly, the hardness of the as-deposited nanochannel V500 was significantly higher than that of the as-deposited nanochannel V600. Secondly, after irradiation, the irradiation hardening of the bulk V was larger than thoes of the nanochannel V films.

Radiation hardening is contributed by interactions of dislocations with different types of defects. In the case of the irradiated bulk V, the defect microstructure was dominated by nanometer-scale He bubbles. In addition, the contribution of bubbles to hardening is significant when the He concentration is above a critical value of 1 at.% [51]. The He concentration in our experiment was as high as 10 at.%. Therefore, the irradiation hardening will be interpreted in terms of the pinning of glide dislocations at these bubbles. A hardening relationship developed by Friedel–Kroupa–Hirsch (FKH) was applied to describe the dependence of radiation hardening on He bubbles using the Eq. (3) [4,14].

$$\Delta\sigma = 1/8\, M\, \mu b d N^{2/3} \tag{3}$$

where $\Delta\sigma$ is the increase in yield strength, M is the Taylor factor (taken as 3), the shear modulus μ is 46.7 GPa [52], b is the Burgers vector of the primary glide dislocations and equals to 2.5 nm, d and N are the average bubble diameter and bubble density, respectively. For bubble density measurement, there are many uncertainties when counting the bubbles in two-dimensional TEM images [53]. At room temperature, the state of He depends on the pressure in bubbles. According to the He phase diagram [53,54], the He density was estimated to be 200 atoms/nm^3. According to the method by Wei [53], the average density of He bubbles was calculated to be 0.067/nm^3. Therefore, the increase in yield strength was calculated to be 0.6 Gpa, and the corresponding hardness enhancements was 1.8 GPa in the bulk V assuming that the yield strength was one-third of the hardness in bulk materials. The experimental result of hardness increasment was 2.5 Gpa, indicating that the major factor contributing to hardening was He bubbles. Dislocation loops formed in the bulk V (Fig. 2c) are typically considered as barriers to the trespassing of dislocations. The increase in yield strength induced by dislocations loops can be calculated by the Eq. (4).

$$\Delta\sigma = M\, \alpha \mu b (Nd)^{1/2} \tag{4}$$

where α is the defect cluster barrier strength. As determination of loop density is not available, Li assumed that the radiation hardening in Nb arrived from He bubbles and dislocation loops, then dislocation loop induced hardening should be the difference between the measured hardening and the He bubble induced hardening [6]. Therefore, the dislocation loops induced hardening in the bulk V was 0.7 Gpa, i.e. the difference between 2.5 Gpa and 1.8 Gpa. For the nanochannel V films, due to the small column size, the deformation of columns was controlled by nucleation of dislocations at surfaces as opposed to the motion of the glide dislocations [55]. We firstly discuss the strength of the as-deposited nanochannel V films. The hardness of metals usually increase when the grain size of the material is reduced. This relation, known as the Hall–Petch relation, is believed to be because of the grain boundaries hindering dislocation activity, thereby making plastic deformation more difficult at small grain sizes [56]. However, for grains smaller than a critical

value, a reverse Hall–Petch effect is appeared [57,58]. The plastic deformation is no longer dominated by dislocation motion but is instead carried by atomic sliding in the grain boundaries. The criticle grain size where the breakdown of the Hall–Petch effect occurs was estimated to be in the range from 11 to 50 nm for copper [59,60]. The average grain size of V500 estimated by the TEM images is larger than that of the V600 due to the "vein-like" nanochannel structure of the V600. However, as a kind of nanochannel material, the mechanical properties of the nanochannel V films are controlled by the relative density (property of porous material) and the strength (σ_b) of individual V column (size effect-"smaller is better"). Therefore, it can not be determined only from the hardness value in Table 1 whether the Hall–Petch effect or the reverse Hall–Petch effect works. The yield strengths of nanochannel V can be expressed by the Eq. (5).

$$\sigma = C\sigma_b(1-p)^n \qquad (5)$$

where p is the porosity. Previous experiments by Biener et al. and Li et al. suggested that $C = 0.3$ and $n = 3/2$ [55,61,62]. In nanochannel materials, as the surrounding material does not constrain the deformation of the nanochannel materials under the indenter due to densification, yield stress is equal to hardness as shown in Table 1. The strength of the V column σ_b can be calculated by Eq. (5) to be 16.6 Gpa and 14.9 Gpa for the nanochannel V500 and V600, respectively. Therefore, the high strength of nanochannel material originated from the high strength of individual V column. Many other studies also showed that for nanoporous metals, the nanoligaments were significantly stronger [55,61–63]. The strength of the V column was calculated using the relation (6).

$$\sigma_b = Kd^m \qquad (6)$$

where d is the column size, and equals to 41 and 58 nm for the nanochannel V500 and V600, respectively. K is a constant and m is column size dependent. m is calculated to be -0.3, which is comparable to those of other nanoporous materials [63,64]. Therefore, the strengthening mechanisms in the nanochannel V films are suggested to be the same as those in nanoporous materials. The structure of the irradiated nanochannel V600 was free of vein-like structure, and the relative density of it was 87%. Therefore, the irradiation hardening of nanochannel V600 originated from two parts: the densification of the structure and the irradiation induced defects. The hardness of the as-deposited nanochannel V600 without vein-like structure could be calculated by substitute the relative density of 87% into Eq. (5), which resulted in a hardness value of 3.6 Gpa. The hardening induced by the densification was 3.6 minus 2.9 Gpa, i.e. 0.7 Gpa. As the measured hardening was 1.3 Gpa, the irradiation induced hardening was 0.6 Gpa, which was one fourth of the hardening of the bulk V. The release of defects through the nanochannel structure led to smaller hardening in nanochannel V films. In addition, the vein-like nanochannel structure of the nanochannel V600 would further help the defects to escape and result in the smallest irradiation hardening.

4. Conclusion

In summary, we report on the significant increase of radiation tolerance in the V films with abundant nanochannels. According to the calculated diffusion distances of He interstitials, SIAs and vacancies, we come to the conclusion that He interstitials, SIAs can diffuse out of the V film. The interstitial-rich surfaces can promote the migration of the less-mobile vacancies and play a role in annihilating them. Thus, free surfaces act as efficient sinks for both vacancies and interstitials. The nanochannel V films with a high surface-to-volume ratio has the potential to be extremely radiation tolerant. The fabrication and investigation of the nanochannel film have important significance in identifying key factors governing radiation damage and searching for radiation tolerant materials.

References

[1] A. Kashinath, A. Misra, M.J. Demkowicz, Stable storage of helium in nanoscale platelets at semicoherent interfaces, Phys. Rev. Lett. 110 (2013) 086101.

[2] Y.F. Zhang, C.M. Paul, T. Michael, Z. Liangzhe, B. Bulent, Molecular dynamics simulations of He bubble nucleation at grain boundaries, J. Phys.: Condens. Matter 24 (2012) 305005.

[3] D. Bhattacharyya, M. Demkowicz, Y.Q. Wang, R. Baumer, M. Nastasi, A. Misra, A transmission electron microscopy study of the effect of interfaces on bubble formation in he-implanted Cu-Nb multilayers, Microsc. Microanal. 18 (2012) 152–161.

[4] N. Li, E.G. Fu, H. Wang, J. Carter, L. Shao, S. Maloy, A. Misra, X. Zhang, He ion irradiation damage in Fe/W nanolayer films, J. Nucl. Mater. 389 (2009) 233–238.

[5] X. Zhang, N. Li, O. Anderoglu, H. Wang, J. Swadener, T. Höchbauer, A. Misra, R. Hoagland, Nanostructured Cu/Nb multilayers subjected to helium ion-irradiation, Nucl. Instrum. Methods Phys. Res., Sect. B 261 (2007) 1129–1132.

[6] A. Misra, N. Li, M. Martin, O. Anderoglu, L. Shao, H. Wang, X. Zhang, He ion irradiation damage to Al/Nb multilayers, J. Appl. Phys. 105 (2009) 123522.

[7] E.G. Fu, A. Misra, H. Wang, L. Shao, X. Zhang, Interface enabled defects reduction in helium ion irradiated Cu/V nanolayers, J. Nucl. Mater. 407 (2010) 178–188.

[8] K. Hattar, M. Demkowicz, A. Misra, I. Robertson, R. Hoagland, Arrest of He bubble growth in Cu–Nb multilayer nanocomposites, Scr. Mater. 58 (2008) 541–544.

[9] X.M. Bai, A.F. Voter, R.G. Hoagland, M. Nastasi, B.P. Uberuaga, Efficient annealing of radiation damage near grain boundaries via interstitial emission, Science 327 (2010) 1631–1634.

[10] M. Samaras, P. Derlet, H. Van Swygenhoven, M. Victoria, Computer simulation of displacement cascades in nanocrystalline Ni, Phys. Rev. Lett. 88 (2002) 125505.

[11] T. Shen, Radiation tolerance in a nanostructure: is smaller better?, Nucl Instrum. Methods Phys. Res., Sect. B 266 (2008) 921–925.

[12] M.J. Demkowicz, R.G. Hoagland, B.P. Uberuaga, A. Misra, Influence of interface sink strength on the reduction of radiation-induced defect concentrations and fluxes in materials with large interface area per unit volume, Phys. Rev. B 84 (2011) 104102.

[13] T. Hochbauer, A. Misra, K. Hattar, R. Hoagland, Influence of interfaces on the storage of ion-implanted He in multilayered metallic composites, J. Appl. Phys. 98 (2005) 123516.

[14] E.G. Fu, J. Carter, G. Swadener, A. Misra, L. Shao, H. Wang, X. Zhang, Size dependent enhancement of helium ion irradiation tolerance in sputtered Cu/V nanolaminates, J. Nucl. Mater. 385 (2009) 629–632.

[15] M.Q. Hong, F. Ren, H.X. Zhang, X.H. Xiao, B. Yang, C.X. Tian, D.J. Fu, Y.Q. Wang, C.Z. Jiang, Enhanced radiation tolerance in nitride multilayered nanofilms with small period-thicknesses, Appl. Phys. Lett. 101 (2012) 153117.

[16] B. Singh, On the influence of grain boundaries on void growth, Philos. Mag. 28 (1973) 1409–1413.

[17] E. Bringa, J. Monk, A. Caro, A. Misra, L. Zepeda-Ruiz, M. Duchaineau, F. Abraham, M. Nastasi, S. Picraux, Y. Wang, Are nanoporous materials radiation resistant?, Nano Lett 12 (2011) 3351–3355.

[18] E. Fu, M. Caro, L. Zepeda-Ruiz, Y. Wang, K. Baldwin, E. Bringa, M. Nastasi, A. Caro, Surface effects on the radiation response of nanoporous Au foams, Appl. Phys. Lett. 101 (2012) 191607.

[19] I. Takagi, N. Matsubara, M. Akiyoshi, T. Sasaki, K. Moritani, H. Moriyama, Production and annihilation of deuterium traps in He-irradiated vanadium, J. Nucl. Mater. 363 (2007) 955–959.

[20] I. Mukouda, Y. Shimomura, D. Yamaki, T. Nakazawa, T. Aruga, S. Jitsukawa, Microstructure in vanadium irradiated by simultaneous multi-ion beam of hydrogen, helium and nickel ions, J. Nucl. Mater. 307 (2002) 412–415.

[21] R.H. Li, P.B. Zhang, X.Q. Li, C. Zhang, J.J. Zhao, First-principles study of the behavior of O, N and C impurities in vanadium solids, J. Nucl. Mater. 435 (2013) 71–76.

[22] H. Kuroiwa, K.-I. Fukumoto, M. Narui, H. Matsui, X. Qiu, Mechanical properties of neutron-irradiated vanadium alloys in a liquid-sodium environment, J. Nucl. Mater. 386 (2009) 594–597.

[23] P. Chidambaram, G. Edwards, D. Olson, A thermodynamic criterion to predict wettability at metal-alumina interfaces, Metall. Trans. B 23 (1992) 215–222.
[24] K. Nakajima, T. Ujihara, N. Usami, K. Fujiwara, G. Sazaki, T. Shishido, Phase diagram of growth mode for the SiGe/Si heterostructure system with misfit dislocations, J. Cryst. Growth 260 (2004) 372–383.
[25] P. Politi, G. Grenet, A. Marty, A. Ponchet, J. Villain, Instabilities in crystal growth by atomic or molecular beams, Phys. Rep. 324 (2000) 271–404.
[26] L. Vitos, A. Ruban, H.L. Skriver, J. Kollar, The surface energy of metals, Surf. Sci. 411 (1998) 186–202.
[27] Q. Wei, A. Misra, Transmission electron microscopy study of the microstructure and crystallographic orientation relationships in V/Ag multilayers, Acta Mater. 58 (2010) 4871–4882.
[28] P. Fenter, T. Gustafsson, Structure and morphology of Au grown on Ag (110), Phys. Rev. B 43 (1991) 12195.
[29] F. Ying, R.W. Smith, D.J. Srolovitz, The mechanism of texture formation during film growth: the roles of preferential sputtering and shadowing, Appl. Phys. Lett. 69 (1996) 3007–3009.
[30] G. Bales, A. Zangwill, Macroscopic model for columnar growth of amorphous films by sputter deposition, J. Vac. Sci. Technol., A 9 (1991) 145–149.
[31] H. Trinkaus, B. Singh, Helium accumulation in metals during irradiation – where do we stand?, J Nucl. Mater. 323 (2003) 229–242.
[32] Q. Wei, Y. Wang, M. Nastasi, A. Misra, Nucleation and growth of bubbles in He ion-implanted V/Ag multilayers, Philos. Mag. 91 (2011) 553–573.
[33] K. Hattar, M. Demkowicz, A. Misra, I. Robertson, R. Hoagland, Arrest of He bubble growth in Cu–Nb multilayer nanocomposites, Scripta Mater. 58 (7) (2008) 541–544.
[34] R.E. Voskoboinikov, Y.N. Osetsky, D.J. Bacon, Computer simulation of primary damage creation in displacement cascades in copper. I. Defect creation and cluster statistics, J. Nucl. Mater. 377 (2008) 385–395.
[35] D.J. Bacon, Y.N. Osetsky, R. Stoller, R.E. Voskoboinikov, MD description of damage production in displacement cascades in copper and α-iron, J. Nucl. Mater. 323 (2003) 152–162.
[36] S.L. Dudarev, The non-Arrhenius migration of interstitial defects in bcc transition metals, C.R. Phys. 9 (2008) 409–417.
[37] L.A. Zepeda-Ruiz, J. Rottler, S. Han, G.J. Ackland, R. Car, D.J. Srolovitz, Strongly non-Arrhenius self-interstitial diffusion in vanadium, Phys. Rev. B 70 (2004) 060102.
[38] M.I. Mendelev, S. Han, W.-J. Son, G.J. Ackland, D.J. Srolovitz, Simulation of the interaction between Fe impurities and point defects in V, Phys. Rev. B 76 (2007) 214105.
[39] M. Kiritani, Defect interaction processes controlling the accumulation of defects produced by high energy recoils, J. Nucl. Mater. 251 (1997) 237–251.
[40] M. Kiritani, H. Takata, Dynamic studies of defect mobility using high voltage electron microscopy, J. Nucl. Mater. 69 (1978) 277–309.
[41] S. Han, L.A. Zepeda-Ruiz, G.J. Ackland, R. Car, D.J. Srolovitz, Self-interstitials in V and Mo, Phys. Rev. B 66 (2002) 220101.
[42] L.A. Zepeda-Ruiz, J. Rottler, B.D. Wirth, R. Car, D.J. Srolovitz, Self-interstitial transport in vanadium, Acta Mater. 53 (2005) 1985–1994.
[43] J. Rottler, D.J. Srolovitz, R. Car, Point defect dynamics in bcc metals, Phys. Rev. B 71 (2005) 064109.
[44] M. Kiritani, Similarity and difference between fcc, bcc and hcp metals from the view point of point defect cluster formation, J. Nucl. Mater. 276 (2000) 41–49.
[45] A. Minashin, V. Ryabov, Molecular dynamics calculations of point defect diffusion coefficients in vanadium, J. Nucl. Mater. 233 (1996) 996–998.
[46] P. Zhang, J. Zhao, Y. Qin, B. Wen, Stability and dissolution of helium–vacancy complexes in vanadium solid, J. Nucl. Mater. 419 (2011) 1–8.
[47] K. Urban, A. Seeger, Radiation-induced diffusion of point-defects during low-temperature electron irradiation, Philos Mag 30 (1974) 1395–1418.
[48] M. Kiritani, Electron radiation induced diffusion of point defects in metals, J. Phys. Soc. Jpn. 40 (1976) 1035–1042.
[49] Sun C, Bufford D, Chen Y, Kirk M, Wang Y, Li M, Wang H, Maloy S, Zhang X (2014) In situ study of defect migration kinetics in nanoporous Ag with enhanced radiation tolerance. Scientific reports 4.
[50] P. Zhang, J. Zhao, Y. Qin, B. Wen, Stability and migration property of helium and self defects in vanadium and V–4Cr–4Ti alloy by first-principles, J. Nucl. Mater. 413 (2011) 90–94.
[51] H. Trinkaus, The effect of cascade induced gas resolution on bubble formation in metals, J. Nucl. Mater. 318 (2003) 234–240.
[52] S. Biswas, M. Muringer, C.T. Seldam, 60Pressure dependence of the shear modulus of polycrystalline silver from 77 to 298 K and up to 253 MPa, Phys. Status Solidi A 119 (1990) 63–69.
[53] Q. Wei, N. Li, N. Mara, M. Nastasi, A. Misra, 59 Suppression of irradiation hardening in nanoscale V/Ag multilayers, Acta Mater. 59 (2011) 6331–6340.
[54] H.K. Mao, R.J. Hemley, Y. Wu, A.P. Jephcoat, L.W. Finger, C.S. Zha, W.A. Bassett, High-pressure phase diagram and equation of state of solid helium from single-crystal X-Ray diffraction to 23.3 GPa, Phys. Rev. Lett. 60 (1988) 2649–2652.
[55] H. Li, A. Misra, J.K. Baldwin, S. Picraux, Synthesis and characterization of nanoporous Pt–Ni alloys, Appl. Phys. Lett. 95 (2009) 201902.
[56] J. Schiøtz, K.W. Jacobsen, A maximum in the strength of nanocrystalline copper, Science 301 (2003) 1357–1359.
[57] H. Van Swygenhoven, Grain boundaries and dislocations, Science 296 (2002) 66–67.
[58] J. Schiotz, F.D. Di Tolla, K.W. Jacobsen, Softening of nanocrystalline metals at very small grain sizes, Nature 391 (1998) 561–563.
[59] S. Yip, Nanocrystals: the strongest size, Nature 391 (1998) 532–533.
[60] E. Arzt, Size effects in materials due to microstructural and dimensional constraints: a comparative review, Acta Mater. 46 (1998) 5611–5626.
[61] J. Biener, A.M. Hodge, A.V. Hamza, L.M. Hsiung, J.H. Satcher, Nanoporous Au: a high yield strength material, J. Appl. Phys. 97 (2005) 024301.
[62] J. Biener, A.M. Hodge, J.R. Hayes, C.A. Volkert, L.A. Zepeda-Ruiz, A.V. Hamza, F.F. Abraham, Size effects on the mechanical behavior of nanoporous Au, Nano Lett. 6 (2006) 2379–2382.
[63] M. Hakamada, M. Mabuchi, Mechanical strength of nanoporous gold fabricated by dealloying, Scripta Mater. 56 (2007) 1003–1006.
[64] B. Wu, A. Heidelberg, J.J. Boland, Mechanical properties of ultrahigh-strength gold nanowires, Nat. Mater. 4 (2005) 525–529.